Science Advances
AAAS

Supplementary Materials for

Mafic slab melt contributions to Proterozoic massif-type anorthosites

Duncan S. Keller *et al.*

Corresponding author: Duncan S. Keller, dsk7@rice.edu

Sci. Adv. **10**, eadn3976 (2024)
DOI: 10.1126/sciadv.adn3976

The PDF file includes:

Figs. S1 to S6
Tables S1 to S6
Legends for tables S7 to S15
References

Other Supplementary Material for this manuscript includes the following:

Tables S7 to S15

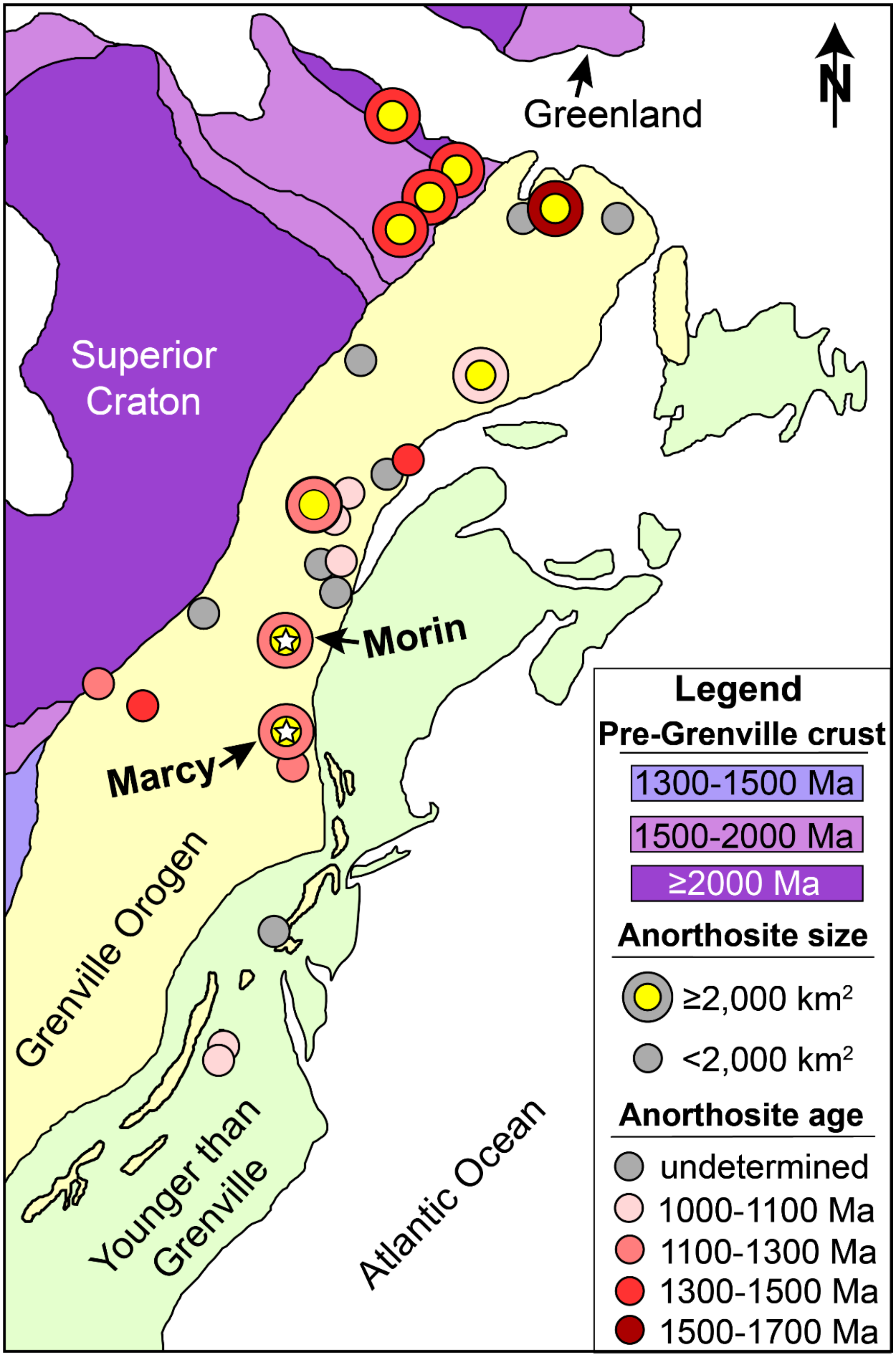

Figure S1. Massif-type anorthosites >5 km^2 of the eastern United States and Canada. Terrane map after ref (130); anorthosite locations after ref (41) and ages are from ref (128).

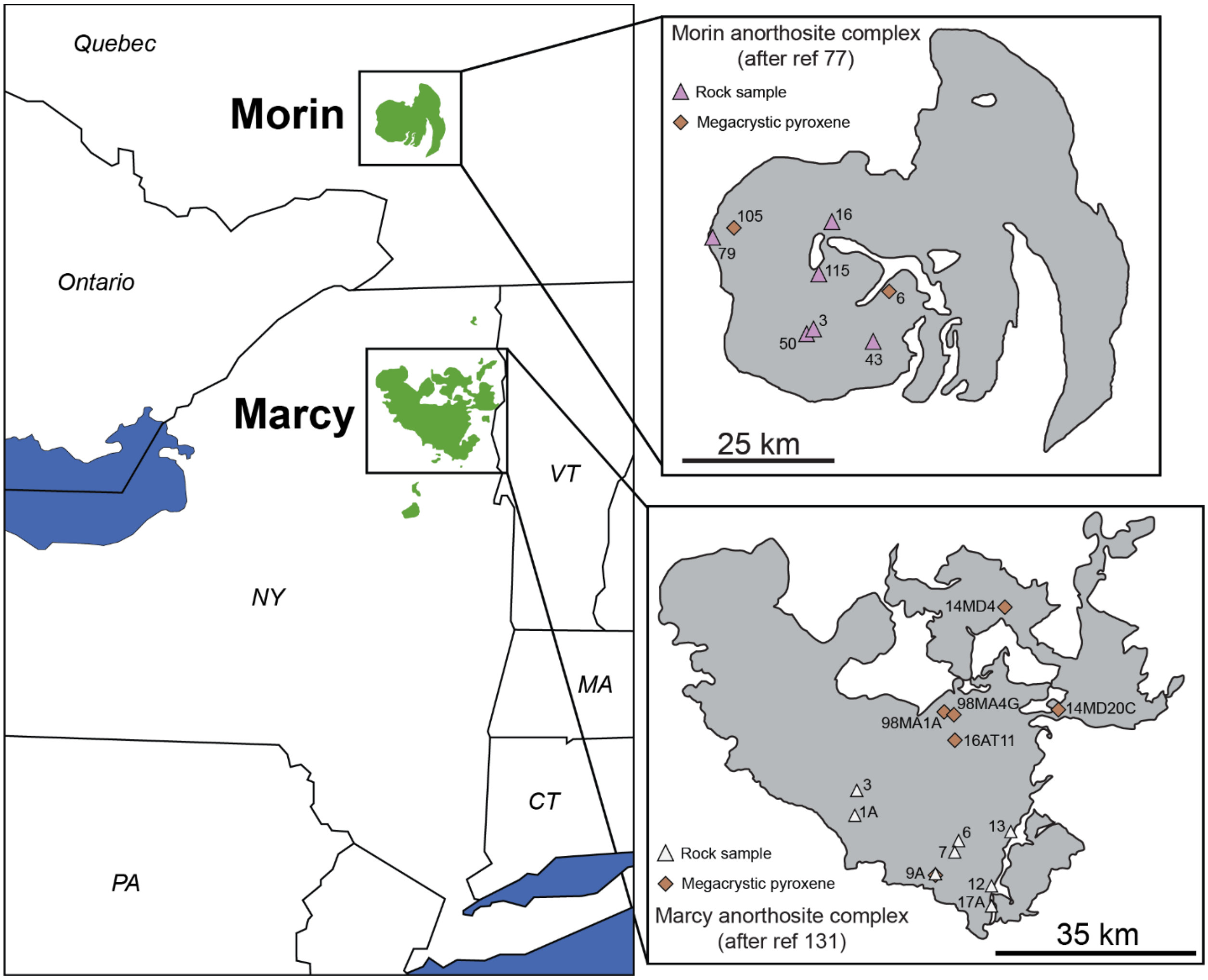

Figure S2. Massif and sample locations. Green outlines represent the main outcroppings of the massifs. Sample locations are marked on inset panels. Morin samples have code prefix 95MR and Marcy samples have code prefix 14AD unless otherwise specified. The Morin map is after ref (77) and the Marcy map is after ref (131).

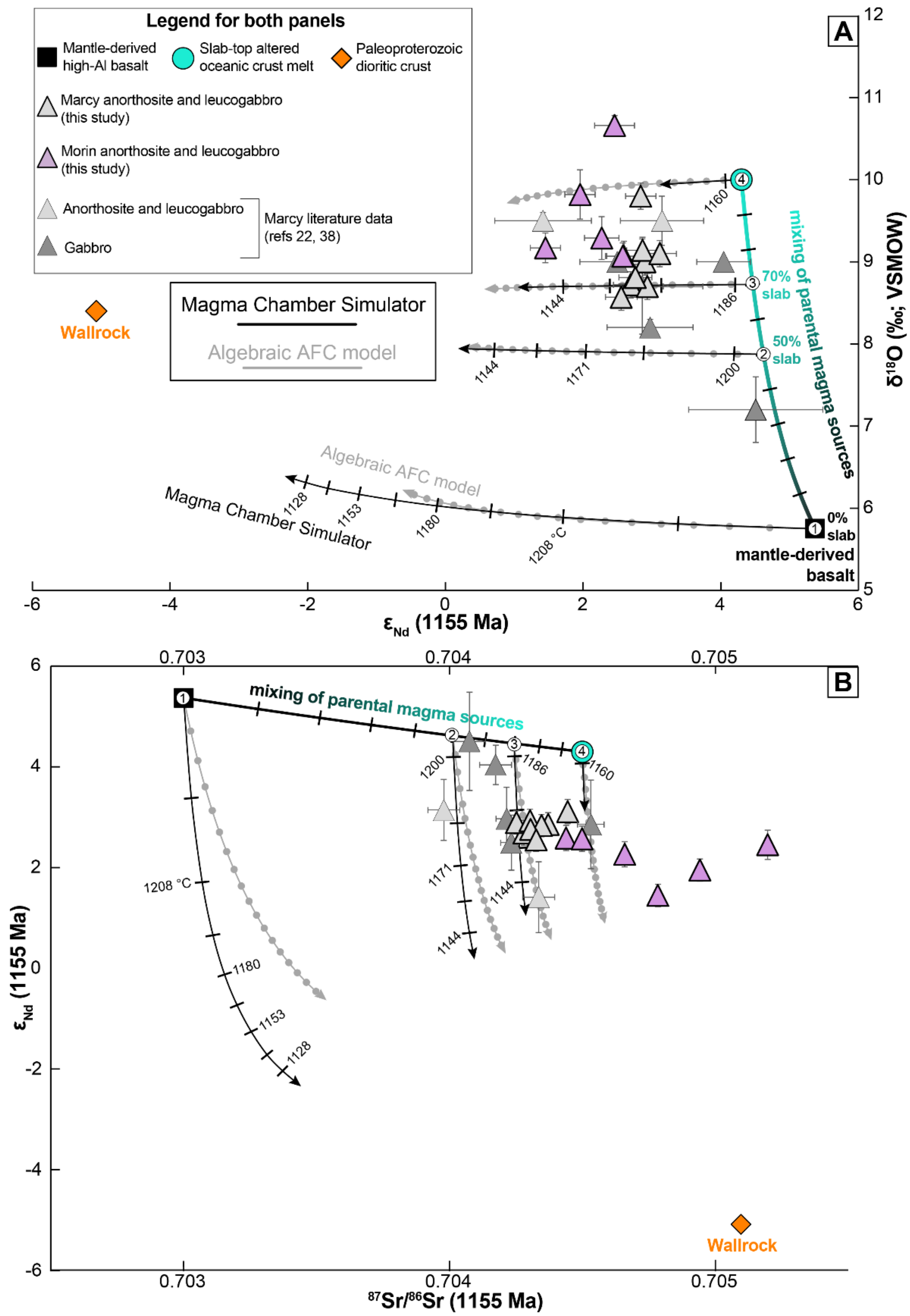

Figure S3. Comparison between Magma Chamber Simulator and assimilation-fractional crystallization (AFC) model results for Nd-Sr-O isotope systematics. Numbers on tick marks of Magma Chamber Simulator curves denote temperature in °C. Circles on AFC curves denote intervals of net 4.5g magma volume decrease from the starting 100g (5g magma volume decrease from crystallization + 0.5g magma volume increase from assimilation).

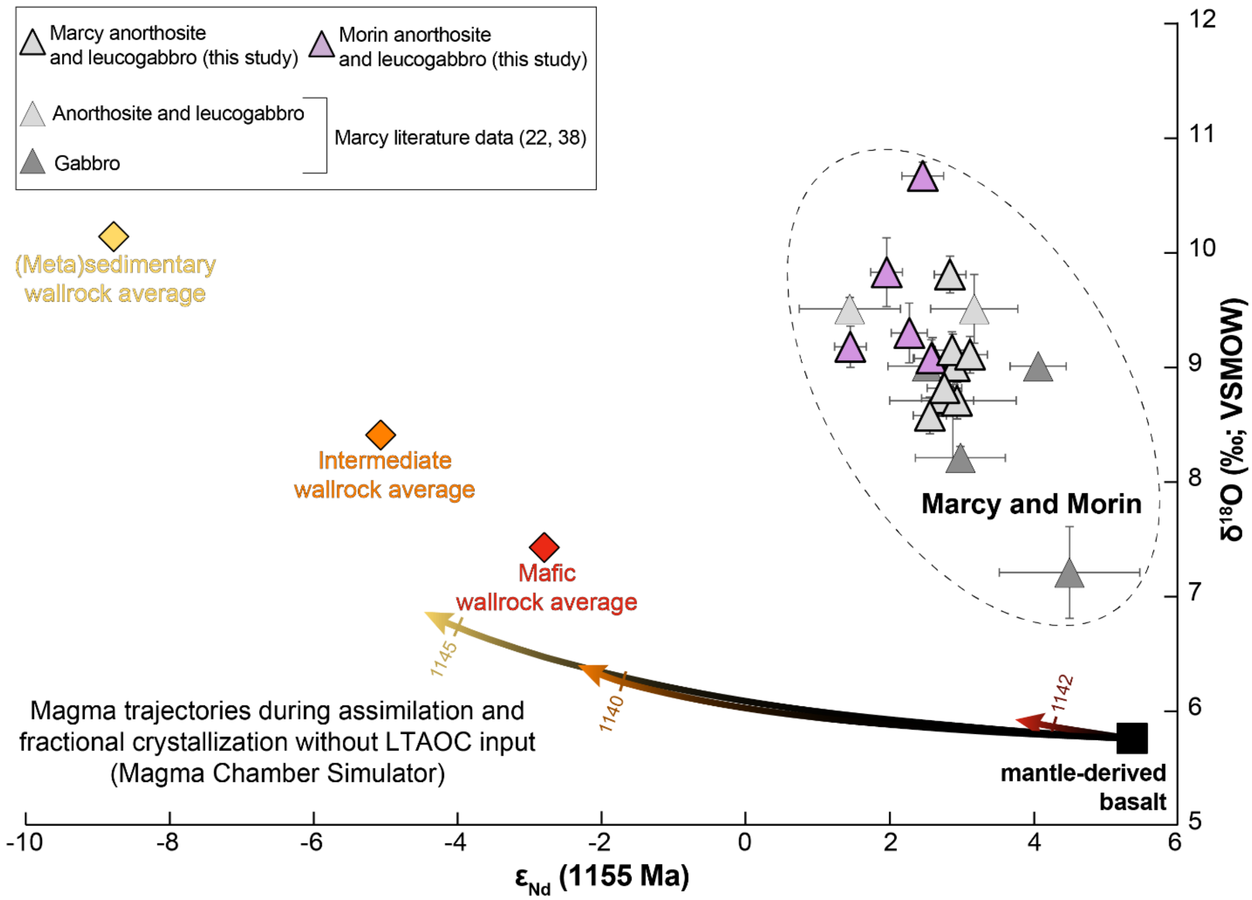

Figure S4. Comparison of magma Nd-O systematics from Magma Chamber Simulator runs of mantle-derived basalt assimilating various wallrock types without LTAOC input. The run with mantle-derived basalt assimilating intermediate crust is the same as in Figure 4.

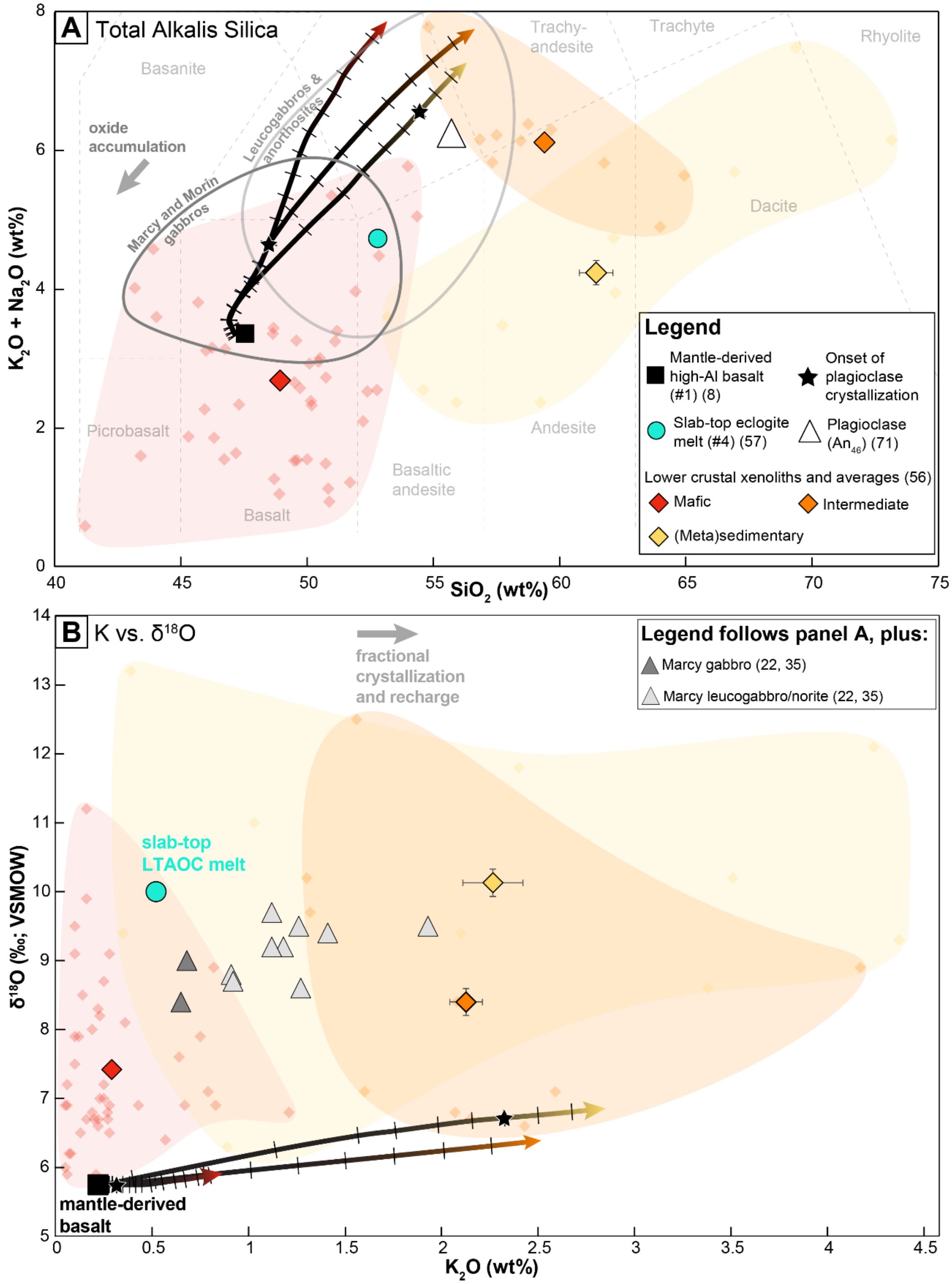

Figure S5. Marcy and Morin major elements and plagioclase compositions compared to Magma Chamber Simulator results for runs without LTAOC melt. Stars show the onset of plagioclase crystallization. The run with mantle-derived basalt assimilating intermediate crust is the same as in Figure 5.

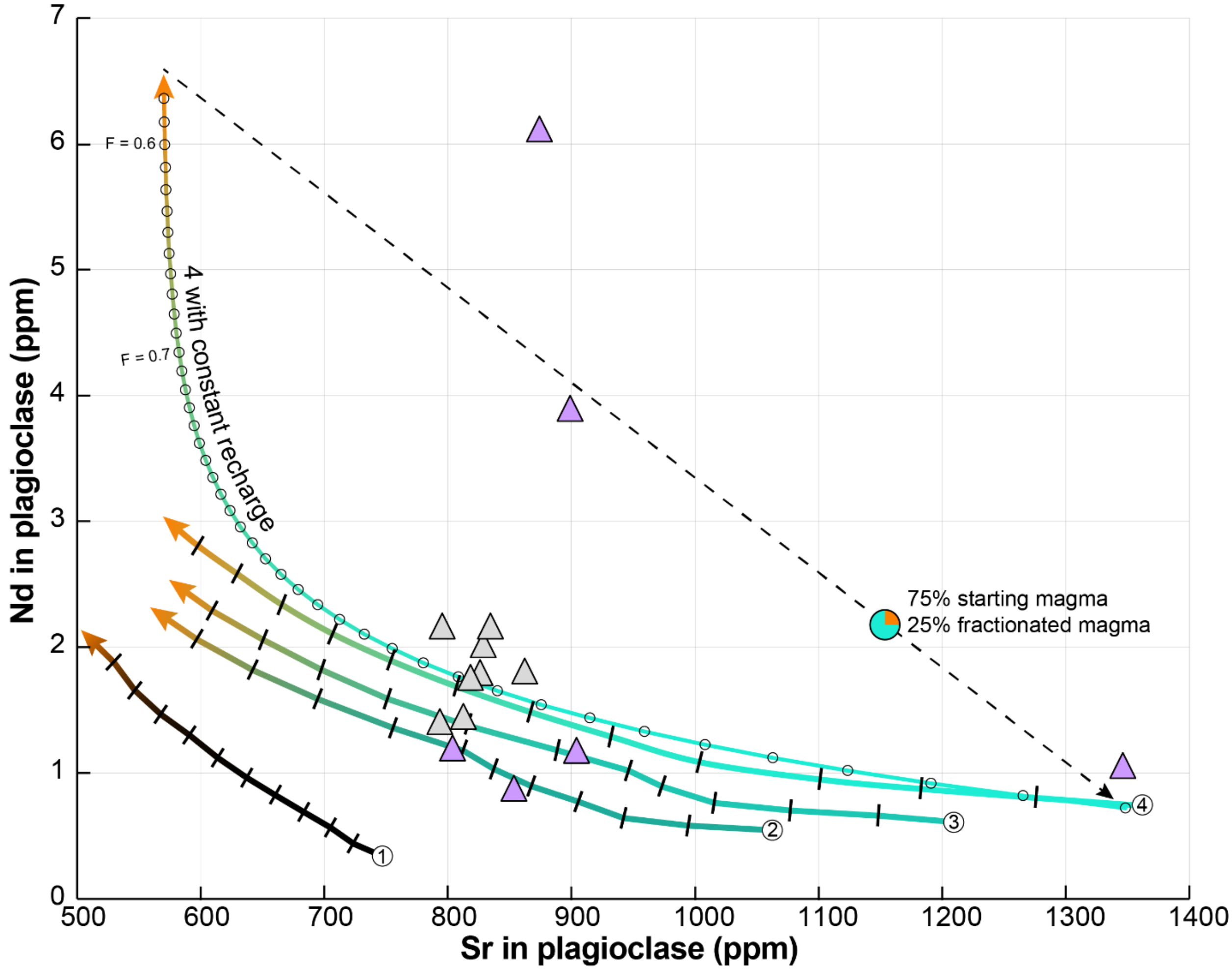

Figure S6. Modelling of Nd and Sr concentrations in cumulus plagioclase. Crystallization trajectories of candidate parental magmas #1-4 during assimilation and fractional crystallization (AFC) are shown from Tables S10-S13 and reproduce the least evolved values in plagioclase. Tick marks correspond to those in Fig. 4. Also shown is an algebraic AFC model (method of Table S9) based on candidate parental magma #4 but with constant recharge equivalent in mass to the amount of assimilated material at each step (2g of each for each 5g of crystallization); each small circle denotes 1% net crystallization. The concentration of an incompatible trace element (Nd) increases during recharge until it reaches a quasi-steady state (54). Mixing of fractionally crystallized magma with fresh magma can produce higher Nd contents in plagioclase than one-step crystallization of a single batch of magma.

Table S1. Boron isotopic data for whole grains analyzed by SIMS at Woods Hole Oceanographic Institution (WHOI) and LA-MC-ICP-MS at Lamont-Doherty Earth Observatory (LDEO). Grain averages were calculated from individual measurements given in Table S2. All grains are plotted in Figure 3 except those labelled “altered or uncertain.”

	Plagioclase	**B (ppm)**	**2σ stderr**	**δ^{11}B (‰)**	**2σ stderr**	**N**
WHOI	14AD1A plag 2	1.04	0.01	-1.0	2.2	5
	14AD3 plag 1	0.60	0.01	-0.9	3.8	5
	14AD3 plag 2	0.70	0.01	-1.6	4.0	5
	14AD9A plag 1	1.13	0.05	-3.4	2.6	4
	14AD13 clean plag 1	1.86	0.02	-0.2	1.2	5
	95MR43 plag	0.92	0.02	-1.0	1.1	5
	95MR115 plag 1	1.18	0.06	-2.5	1.4	5
LDEO	14AD9A section 2 plag 1	0.41	0.04	-14.5	2.0	3
	14AD9A section 2 plag 2	0.37	0.02	-23.2	4.3	4
	14AD9A section 2 plag 3	0.44	0.05	-20.5	3.0	2
	14AD9A section 2 plag 4	0.39	0.02	-22.2	1.2	3
	14AD9A section 2 plag 5	0.45	0.01	-5.5	1.7	4
	14AD9A section 2 plag 6	0.42	0.01	-5.5	2.8	3
	Pyroxene	**B (ppm)**	**2σ stderr**	**δ^{11}B (‰)**	**2σ stderr**	**N**
WHOI	14AD9A_littlepyx	4.34	0.29	11.4	1.4	3
	14AD13	2.67	0.73	5.3	1.8	6
	95MR115 pyx 1	1.30	0.05	-0.5	0.4	4
	95MR115 pyx 2	1.35	0.15	-1.4	4.5	3
LDEO	14AD9A_pyxrim	1.22	0.07	0.9	0.5	6
	14AD9A_littlepyx	3.13	1.06	11.4	0.1	2
	Megacrystic pyroxene	**B (ppm)**	**2σ stderr**	**δ^{11}B (‰)**	**2σ stderr**	**N**
WHOI	95MR105_R	0.51	0.06	9.1	1.0	5
	14MD20C_R	1.17	0.07	7.2	1.7	5
	16AT11	1.77	0.07	-4.8	1.5	5
	98MA4G_R	0.49	0.03	9.4	2.3	6
	98MA1A	14.95	0.65	2.5	1.3	5
	95MR6	0.89	0.04	-0.5	2.0	5
LDEO	14AD9A_HAOM1adjcpx	5.04	1.88	21.0	3.2	4
	98MA1A	18.65	0.46	8.0	1.7	8
	Altered or uncertain	**B (ppm)**	**2σ stderr**	**δ^{11}B (‰)**	**2σ stderr**	**N**
WHOI	14AD13 altered plag 1	2.11	0.42	5.4	2.4	4
	14AD17A plag 1	1.14	0.02	-3.3	1.3	5
	14AD17A plag 2	1.59	0.05	-0.8	1.6	4
	14AD17A plag 3	2.71	0.07	2.7	1.3	5
	14AD1A pyx/amph1	2.19	0.82	2.6	8.8	3
	14MD4	2.58	0.26	-2.3	3.2	5
	14AD9A_HAOM1_WHOI	51.91	6.10	33.5	3.3	3
LDEO	14AD9A-HAOM1	52.96	23.17	30.3	1.7	9

Table S2. Individual spot analyses of boron isotopic data analyzed by SIMS at Woods Hole Oceanographic Institution (WHOI) and LA-MC-ICP-MS at Lamont-Doherty Earth Observatory (LDEO). Italicized analyses are those with 1σ standard error ≥5‰ and are excluded from the grain averages in Table S1. For LDEO data, values in parentheses are $\delta^{11}B$ values and uncertainties before the application of a spot size correction. Plagioclase grains in sample 14AD17A contain fine-grained unidentified inclusions and/or amphibole inclusions of ambiguous origin, although analyzed areas do not show clear signs of alteration. *Field aperture was set to 15000 µm x 15000 µm instead of 4000 µm x 4000 µm for this analysis (see Materials and Methods).

Lab	Plagioclase	B (ppm)	2σ stdev	$\delta^{11}B$ (‰)	2σ stderr
WHOI	14AD1A_plag 2_spot1	1.04	0.08	-0.6	4.7
	14AD1A_plag 2_spot2	1.03	0.08	2.5	3.5
	14AD1A_plag 2_spot3	1.04	0.10	-3.6	5.0
	14AD1A_plag 2_spot4	1.04	0.09	-3.2	5.4
	14AD1A_plag 2_spot5	1.05	0.10	0.0	3.8
	14AD3_plag1_spot1	0.60	0.03	-6.8	6.1
	14AD3_plag1_spot2	0.60	0.03	-0.9	3.7
	14AD3_plag1_spot3	0.59	0.03	-2.9	5.6
	14AD3_plag1_spot4	0.61	0.02	3.8	3.5
	14AD3_plag1_spot5	0.60	0.03	2.2	4.9
	14AD3_plag2_spot1	0.72	0.08	-7.1	3.6
	14AD3_plag2_spot2	0.67	0.06	-1.7	5.0
	14AD3_plag2_spot3	0.70	0.06	-0.7	3.9
	14AD3_plag2_spot4	0.70	0.06	-3.6	3.8
	14AD3_plag2_spot5	0.70	0.06	5.2	4.4
	14AD9A_plag1_spot1	1.12	0.10	-3.0	3.9
	14AD9A_plag1_spot2	1.09	0.08	-4.0	4.7
	14AD9A_plag1_spot3	1.21	0.12	-0.2	4.5
	14AD9A_plag1_spot4	1.12	0.09	-6.4	4.6
	14AD9A_plag1_spot5	*1.12*	*0.13*	*-11.3*	*10.8*
	14AD13_plag1_spot1	1.89	0.09	0.4	4.4
	14AD13_plag1_spot2	1.88	0.09	-1.8	4.3
	14AD13_plag1_spot3	1.86	0.08	-0.9	3.9
	14AD13_plag1_spot4	1.83	0.07	-0.3	3.4
	14AD13_plag1_spot5	1.85	0.07	1.6	3.6
	95MR43_plag1_spot1	0.88	0.02	-0.5	2.8
	95MR43_plag1_spot2	0.92	0.03	-1.7	2.9
	95MR43_plag1_spot3	0.94	0.04	-2.6	2.6
	95MR43_plag1_spot4	0.95	0.03	0.7	2.1
	95MR43_plag1_spot5	0.91	0.03	-0.9	3.2
	95MR115_plag1_spot1	1.21	0.11	-5.0	3.9
	95MR115_plag1_spot2	1.25	0.13	-3.0	4.2
	95MR115_plag1_spot3	1.08	0.19	-1.2	4.4

Lab	Plagioclase (cont.)	B (ppm)	2σ stdev	$\delta^{11}B$ (‰)	2σ stderr
WHOI	95MR115_plag1_spot4	1.18	0.07	-1.3	4.4
	95MR115_plag1_spot5	1.16	0.07	-2.1	3.6
LDEO	14AD9A_FTS_plag1_9low	0.42	semiquant	-15.2 (-16.2)	6.3 (5.7)
	14AD9A_FTS_plag1_11	0.38	semiquant	-12.5 (-13.6)	6.1 (5.6)
	14AD9A_FTS_plag1_12	0.45	semiquant	-15.7 (-16.7)	4.0 (2.6)
	14AD9A_FTS_plag2_13	0.35	semiquant	-19.3 (-20.4)	3.4 (2.5)
	14AD9A_FTS_plag2_14	0.40	semiquant	-20.5 (-18.3)	3.7 (3.4)
	14AD9A_FTS_plag2_15	0.37	semiquant	-28.7 (-26.5)	3.5 (3.1)
	14AD9A_FTS_plag2_18	0.37	semiquant	-24.5 (-22.2)	4.6 (4.3)
	14AD9A_FTS_plag3_16	0.42	semiquant	-19.0 (-16.8)	3.4 (3.0)
	14AD9A_FTS_plag3_17	0.47	semiquant	-22.0 (-20.0)	3.6 (3.1)
	14AD9A_FTS_plag4_19	0.38	semiquant	-23.0 (-20.8)	4.5 (4.2)
	14AD9A_FTS_plag4_20	0.41	semiquant	-21.0 (-18.9)	4.5 (4.2)
	14AD9A_FTS_plag4_21	0.39	semiquant	-22.4 (-20.2)	4.6 (4.3)
	14AD9A_FTS_plag5_26	0.43	semiquant	-3.7 (-1.6)	6.1 (5.9)
	14AD9A_FTS_plag5_27	0.45	semiquant	-5.8 (-3.7)	6.1 (5.8)
	14AD9A_FTS_plag5_28	0.46	semiquant	-4.9 (-2.9)	6.1 (5.9)
	14AD9A_FTS_plag5_29	0.44	semiquant	-7.6 (-5.6)	6.1 (5.8)
	14AD9A_FTS_plag6_30	0.41	semiquant	-7.9 (-5.8)	2.4 (1.8)
	14AD9A_FTS_plag6_31	0.42	semiquant	-5.7 (-3.6)	2.2 (1.4)
	14AD9A_FTS_plag6_32	0.42	semiquant	-3.0 (-0.9)	3.8 (3.4)
Lab	**Pyroxene**	**B (ppm)**	**2σ stdev**	**$\delta^{11}B$ (‰)**	**2σ stderr**
WHOI	14AD9A_littlepyx_WHOI_spot1	4.07	0.41	11.1	2.8
	14AD9A_littlepyx_WHOI_spot2	4.39	0.76	10.5	2.8
	14AD9A_littlepyx_WHOI_spot3	4.57	0.44	12.7	3.4
	14AD13_pyx1_spot1	1.99	0.11	1.7	4.1
	14AD13_pyx1_spot2	2.65	0.29	4.3	2.7
	14AD13_pyx1_spot3	2.37	0.18	5.6	2.4
	14AD13_pyx1_spot4	2.89	1.96	6.6	2.9
	14AD13_pyx1_spot5	1.84	0.12	5.2	3.7
	14AD13_pyx1_spot6	4.30	0.42	8.3	3.3
	95MR115_ pyx1_spot1	1.30	0.09	0.0	3.8
	95MR115_ pyx1_spot2	1.26	0.07	-0.6	4.1
	95MR115_ pyx1_spot3	1.36	0.08	-0.5	3.2
	95MR115_ pyx1_spot4	1.26	0.07	-1.0	3.1
	95MR115_ pyx2_spot1	1.35	0.05	-3.4	3.9
	95MR115_ pyx2_spot2	1.48	0.19	-3.8	4.5
	95MR115_ pyx2_spot3	1.21	0.07	3.1	3.9
LDEO	*14AD9A-HAOM-pyxrim_10*	*1.79*	*semiquant*	*1.8 (1.6)*	*18.5 (4.0)*
	14AD9A-HAOM-pyxrim_11	1.27	semiquant	0.4 (-0.5)	5.0 (4.1)
	14AD9A-HAOM-pyxrim_12	1.15	semiquant	1.6 (0.5)	4.0 (3.2)
	14AD9A-HAOM-pyxrim_14	1.10	semiquant	1.5 (0.4)	3.5 (2.8)

Lab	Pyroxene (cont.)	B (ppm)	2σ stdev	$\delta^{11}B$ (‰)	2σ stderr
LDEO	14AD9A_FTS_pyxrim_6	1.30	semiquant	0.6 (-0.1)	8.2 (6.8)
	14AD9A_FTS_pyxrim_7	1.30	semiquant	0.9 (0.2)	8.1 (6.7)
	14AD9A_FTS_pyxrim_8	1.24	semiquant	0.1 (-0.6)	7.9 (6.8)
	14AD9A-littlepyx_15	3.66	semiquant	11.4 (13.8)	3.3 (2.9)
	14AD9A-littlepyx_16	2.60	semiquant	11.4 (12.4)	4.7 (3.1)
Lab	**Megacrystic pyroxene**	**B (ppm)**	**2σ stdev**	**$\delta^{11}B$ (‰)**	**2σ stderr**
WHOI	95MR105_R_WHOI_spot1	0.62	0.06	10.3	4.8
	95MR105_R_WHOI_spot2	0.49	0.02	8.4	4.7
	95MR105_R_WHOI_spot3	0.48	0.02	8.7	6.2
	95MR105_R_WHOI_spot4	0.47	0.02	10.2	4.4
	95MR105_R_WHOI_spot5	0.46	0.02	7.7	5.5
	14MD20C_R_WHOI_spot1	1.07	0.04	9.9	4.0
	14MD20C_R_WHOI_spot2	1.13	0.04	4.5	3.6
	14MD20C_R_WHOI_spot3	1.20	0.07	6.7	3.6
	14MD20C_R_WHOI_spot4	1.28	0.04	7.1	3.5
	14MD20C_R_WHOI_spot5	1.18	0.04	7.7	3.9
	16AT11_spot1	1.83	0.07	-5.6	3.7
	16AT11_spot2	1.77	0.06	-3.1	3.6
	16AT11_spot3	1.83	0.06	-5.8	3.7
	16AT11_spot4	1.64	0.07	-2.8	3.0
	16AT11_spot5	1.77	0.06	-6.5	3.1
	98MA4G_R_spot1	0.57	0.05	7.2	5.9
	98MA4G_R_spot2	0.48	0.02	8.0	4.5
	98MA4G_R_spot3	0.48	0.02	15.0	4.7
	98MA4G_R_spot4	0.48	0.02	7.7	4.8
	98MA4G_R_spot5	0.48	0.02	8.9	4.5
	98MA4G_R_spot6	0.46	0.02	9.6	5.7
	98MA1A_WHOI_spot1	15.64	0.60	1.4	2.2
	98MA1A_WHOI_spot2	14.73	0.50	2.4	2.3
	98MA1A_WHOI_spot3	13.79	0.50	4.5	2.3
	98MA1A_WHOI_spot4	15.73	0.56	0.9	2.3
	98MA1A_WHOI_spot5	15.22	0.56	3.4	2.4
	95MR6_spot1	0.86	0.04	0.9	4.7
	95MR6_spot2	0.92	0.05	0.1	4.4
	95MR6_spot3	0.84	0.04	-1.5	4.5
	95MR6_spot4	0.88	0.04	-4.0	4.2
	95MR6_spot5	0.96	0.04	1.9	4.2
LDEO	14AD9A_FTS_HAOM1adjcpx_22	4.96	semiquant	19.3 (15.9)	4.8 (4.3)
	14AD9A_FTS_HAOM1adjcpx_23	7.48	semiquant	23.9 (20.0)	4.7 (4.3)
	14AD9A_FTS_HAOM1adjcpx_24	4.84	semiquant	23.4 (22.0)	6.1 (4.3)
	14AD9A_FTS_HAOM1adjcpx_25	2.88	semiquant	17.4 (18.0)	9.0 (5.0)
	98MA1A_1	18.96	semiquant	3.1 (11.7)	1.55 (1.3)

Lab	Megacrystic pyroxene (cont.)	B (ppm)	2σ stdev	$\delta^{11}B$ (‰)	2σ stderr
LDEO	98MA1A_2	19.61	semiquant	9.2 (13.4)	1.72 (1.3)
	98MA1A_3	19.47	semiquant	9.4 (13.6)	1.73 (1.3)
	98MA1A_4	18.25	semiquant	8.5 (12.2)	1.88 (1.4)
	98MA1A_5	17.90	semiquant	5.8 (9.4)	1.97 (1.5)
	98MA1A_6	18.65	semiquant	7.8 (11.6)	1.92 (1.5)
	98MA1A_7	18.02	semiquant	9.9 (11.3)	3.15 (1.8)
	98MA1A_8	18.35	semiquant	10.4 (11.8)	3.17 (2.0)
Lab	**Altered or uncertain grains**	**B (ppm)**	**2σ stdev**	**$\delta^{11}B$ (‰)**	**2σ stderr**
WHOI	14AD13_alteredplag1_spot1	2.70	0.09	6.6	2.4
	14AD13_alteredplag1_spot2	1.78	0.09	3.2	3.8
	14AD13_alteredplag1_spot3	1.83	0.09	3.6	3.2
	14AD13_alteredplag1_spot4	2.12	0.06	8.3	3.7
	14AD17A_plag1_spot1	1.14	0.02	-3.7	2.8
	14AD17A_plag1_spot2	1.14	0.02	-5.6	3.6
	14AD17A_plag1_spot3	1.17	0.02	-1.7	3.3
	14AD17A_plag1_spot4	1.12	0.03	-2.8	3.3
	14AD17A_plag1_spot5	1.12	0.04	-2.4	3.4
	14AD17A_plag2_spot1	1.66	0.02	0.0	2.8
	14AD17A_plag2_spot2	1.58	0.02	-2.6	2.9
	14AD17A_plag2_spot3	1.60	0.03	1.0	3.1
	14AD17A_plag2_spot4	1.53	0.04	-1.5	2.7
	14AD17A_plag3_spot1	2.72	0.21	3.6	3.3
	14AD17A_plag3_spot2	2.78	0.26	3.9	3.9
	14AD17A_plag3_spot3	2.77	0.31	2.1	3.7
	14AD17A_plag3_spot4	2.67	0.36	3.7	3.4
	14AD17A_plag3_spot5	2.60	0.34	0.5	3.6
	14AD1A_pyx/amph1_spot1	2.15	0.24	4.6	2.8
	14AD1A_ pyx/amph1_spot2	2.92	0.37	8.9	3.0
	14AD1A_ pyx/amph1_spot3	1.51	0.22	-5.8	4.5
	14AD17A pyx/amph (only 1 spot)	3.31	N.A.	11.0	N.A.
	14MD4_spot1	2.93	0.10	-3.5	2.6
	14MD4_spot2	2.58	0.10	-3.5	2.6
	14MD4_spot3	2.54	0.11	-2.6	2.7
	14MD4_spot4	2.72	0.11	3.7	2.6
	14MD4_spot5	2.14	0.09	-5.7	2.9
	14AD9A_HAOM1_WHOI_spot1*	54.02	0.70	30.7	2.5
	14AD9A_HAOM1_WHOI_spot2	45.90	1.45	36.5	2.9
	14AD9A_HAOM1_WHOI_spot3	55.82	1.42	33.3	2.5
LDEO	14AD9A-HAOM1_1	141.87	semiquant	29.3 (28.6)	6.1 (4.6)
	14AD9A-HAOM1_2	38.03	semiquant	29.2 (29.8)	7.2 (5.2)
	14AD9A-HAOM1_2b	*39.34*	*semiquant*	*29.2 (30.0)*	*6.2 (4.4)*
	14AD9A-HAOM1_3	22.79	semiquant	29.7 (29.0)	6.2 (4.7)

Lab	Altered or uncertain grains (cont.)	B (ppm)	2σ stdev	δ¹¹B (‰)	2σ stderr
LDEO	*14AD9A-HAOM1_6*	*25.38*	*semiquant*	*27.6 (27.1)*	*11.4 (9.4)*
	14AD9A-HAOM1_7	*28.63*	*semiquant*	*36.7 (36.5)*	*20.1 (9.2)*
	14AD9A-HAOM1_8	38.10	semiquant	25.8 (26.5)	6.3 (3.9)
	14AD9A-HAOM1_9	34.77	semiquant	27.9 (28.2)	9.5 (4.0)
	14AD9A-HAOM1_13	*32.48*	*semiquant*	*29.8 (30.0)*	*19.0 (2.4)*
	14AD9A_FTS_HAOM1_1	48.38	semiquant	33.0 (33.9)	5.3 (2.7)
	14AD9A_FTS_HAOM1_2	*39.58*	*semiquant*	*32.5 (33.0)*	*11.9 (7.0)*
	14AD9A_FTS_HAOM1_3	53.97	semiquant	32.5 (33.8)	4.5 (2.7)
	14AD9A_FTS_HAOM1_3b	52.89	semiquant	31.0 (32.2)	4.6 (2.7)
	14AD9A_FTS_HAOM1_4	45.85	semiquant	34.0 (34.8)	5.9 (2.5)
	14AD9A_FTS_HAOM1_5	*39.05*	*semiquant*	*30.6 (31.0)*	*12.1 (6.7)*

Table S3. Representative unaltered plagioclase chemistry measured by EPMA for grains with boron data in Tables S1 and S2.

Sample	14AD1A plag2	14AD3 plag1	14AD3 plag2	14AD9A plag1	14AD13 clean plag1	95MR43 plag1	95MR115 plag1
SiO_2	55.90	55.89	55.18	55.40	55.72	57.33	58.07
TiO_2	b.d.	0.07	0.04	b.d.	b.d.	0.06	0.03
Al_2O_3	27.76	27.80	28.18	28.23	27.79	26.37	26.34
Cr_2O_3	b.d.	b.d.	0.02	b.d.	0.01	b.d.	0.02
FeO(tot)	0.13	0.14	0.10	0.17	0.14	0.18	0.12
MgO	b.d.	b.d.	0.01	b.d.	0.01	b.d.	b.d.
MnO	0.03	b.d.	0.01	b.d.	b.d.	b.d.	b.d.
CaO	9.85	10.24	10.53	10.80	10.04	8.44	9.00
Na_2O	5.60	5.56	5.25	5.16	5.52	6.54	6.27
K_2O	0.48	0.65	0.63	0.44	0.43	0.44	0.51
Total	**99.76**	**100.35**	**99.95**	**100.20**	**99.65**	**99.35**	**100.36**
Si	2.522	2.513	2.492	2.494	2.517	2.589	2.596
Ti		0.003	0.001			0.002	0.001
Al	1.476	1.473	1.500	1.498	1.480	1.403	1.388
Cr			0.001				0.001
Fe^{2+}	0.005	0.005	0.004	0.006	0.005	0.007	0.005
Mg			0.001		0.001		
Mn	0.001						
Ca	0.476	0.493	0.510	0.521	0.486	0.409	0.431
Na	0.490	0.485	0.460	0.451	0.483	0.572	0.544
K	0.027	0.037	0.036	0.025	0.025	0.026	0.029
Total (8 O)	**4.998**	**5.009**	**5.004**	**4.995**	**4.997**	**5.007**	**4.995**
An (mol%)	**47.9**	**48.6**	**50.7**	**52.3**	**48.9**	**40.6**	**42.9**

Notes: All Fe as FeO. Each grain corresponds to the grain of the same name in Tables S1 and S2; analyses were made proximal to SIMS spots.

Table S4. Representative unaltered pyroxene and megacrystic pyroxene chemistry measured by EPMA for grains with boron data in Tables S1 and S2.

Sample	14AD9A littlepyx	14AD13 pyx1	95MR115 pyx1	95MR115 pyx2	95MR6 Mcpx	98MA1A Mcpx	16AT11 Mcpx	95MR105 Mopx	14MD20C Mopx	98MA4G Mopx
SiO_2	50.16	50.90	53.01	52.95	51.62	52.99	51.60	53.98	53.04	52.98
TiO_2	0.47	0.43	0.47	0.46	0.43	0.31	0.57	0.06	0.10	0.11
Al_2O_3	3.82	3.74	2.96	2.97	2.98	2.38	3.75	1.98	2.03	3.04
Cr_2O_3	b.d.	b.d.	0.05	0.05	b.d.	0.08	0.07	0.04	0.03	0.16
FeO(tot)	12.74	11.72	8.91	9.77	9.32	7.75	8.16	18.38	20.13	18.66
MgO	10.68	10.85	12.45	12.67	13.00	14.06	13.22	25.05	24.05	24.51
MnO	0.26	0.21	0.24	0.22	0.24	0.15	0.23	0.27	0.32	0.31
CaO	21.16	21.78	22.11	21.13	21.84	22.17	21.96	0.33	0.30	0.35
Na_2O	0.47	0.59	0.47	0.46	0.58	0.45	0.49	b.d.	b.d.	b.d.
K_2O	b.d.	b.d.	b.d.	b.d.	b.d.	b.d.	b.d.	b.d.	b.d.	0.01
Total	**99.76**	**100.23**	**100.66**	**100.67**	**100.01**	**100.34**	**100.05**	**100.06**	**99.99**	**100.14**
Si	1.909	1.919	1.959	1.959	1.930	1.956	1.917	1.965	1.951	1.933
Ti	0.013	0.012	0.013	0.013	0.012	0.009	0.016	0.002	0.003	0.003
Al	0.171	0.166	0.129	0.129	0.131	0.104	0.164	0.085	0.088	0.131
Cr			0.001	0.001		0.002	0.002	0.001	0.001	0.005
Fe^{2+}	0.405	0.370	0.275	0.302	0.291	0.239	0.253	0.559	0.619	0.569
Mg	0.606	0.610	0.686	0.698	0.725	0.774	0.732	1.537	1.319	1.333
Mn	0.008	0.007	0.007	0.007	0.008	0.005	0.007	0.008	0.010	0.010
Ca	0.863	0.880	0.876	0.837	0.875	0.877	0.874	0.013	0.012	0.014
Na	0.035	0.043	0.034	0.033	0.042	0.032	0.035			
K										0.001
Total (6 O)	**4.010**	**4.007**	**3.980**	**3.979**	**4.013**	**3.998**	**4.000**	**3.990**	**4.002**	**3.998**

Notes: Prefix “M” denotes megacrystic pyroxene (e.g., “Mopx”) All Fe as FeO. Each grain corresponds to the grain of the same name in Tables S1 and S2; analyses were made proximal to SIMS spots.

Table S5. Neodymium, Sr, and O isotope data for Marcy samples.

Sample	**14AD1A**	**14AD3**	**14AD6**	**14AD7**	**14AD9A**	**14AD12**	**14AD13**	**14AD17A**
Rb (ppm)	0.94	1.19	1.71	0.67	1.63	1.09	1.70	1.30
Sr (ppm)	826.08	793.41	828.48	795.49	834.27	812.53	818.41	862.18
$^{87}Rb/^{86}Sr$	0.00322	0.00426	0.00584	0.00239	0.00553	0.00380	0.00589	0.00428
$^{87}Sr/^{86}Sr$ (measured)	0.704332	0.704321	0.704466	0.704342	0.704436	0.704367	0.704421	0.704513
$^{87}Sr/^{86}Sr$ std error (2σ)	0.000013	0.000013	0.000013	0.000013	0.000013	0.000013	0.000013	0.000013
$^{87}Sr/^{86}Sr$ (1155 Ma)	0.704280	0.704252	0.704371	0.704303	0.704346	0.704305	0.704326	0.704444
Sm (ppm)	0.29	0.25	0.33	0.34	0.33	0.25	0.31	0.27
Nd (ppm)	1.80	1.41	2.02	2.17	2.17	1.45	1.76	1.81
$^{147}Sm/^{144}Nd$	0.09797	0.10629	0.09831	0.09394	0.09248	0.10416	0.10501	0.08865
$^{143}Nd/^{144}Nd$ (measured)	0.512026	0.512100	0.512037	0.512008	0.511992	0.512076	0.512072	0.511977
$^{143}Nd/^{144}Nd$ std error (2σ)	0.000013	0.000012	0.000012	0.000012	0.000011	0.000012	0.000012	0.000012
$^{143}Nd/^{144}Nd$ (1155 Ma)	0.511285	0.511296	0.511294	0.511297	0.511293	0.511289	0.511278	0.511307
ε_{Nd} (1155 Ma)	2.7 ± 0.3	2.9 ± 0.2	2.9 ± 0.2	2.9 ± 0.2	2.8 ± 0.2	2.8 ± 0.2	2.6 ± 0.2	3.1 ± 0.2
$\delta^{18}O$ (VSMOW; ‰)	8.72	9.00	9.14	8.70	9.80	8.81	8.57	9.10
$\delta^{18}O$ std error (2σ; ‰)	0.16	0.16	0.16	0.16	0.16	0.16	0.16	0.16
Boron data in tables S1 and S2 and EPMA data in Tables S3 and/or S4?	Yes	Yes	No	No	Yes	No	Yes	Yes

Table S6. Neodymium, Sr, and O isotope data for Morin samples.

Sample	**95MR3**	**95MR16**	**95MR43**	**95MR50**	**95MR79**	**95MR115**
Rb (ppm)	3.41	2.24	1.98	1.88	5.74	1.60
Sr (ppm)	904.10	873.99	1346.06	853.39	898.94	803.85
$^{87}Rb/^{86}Sr$	0.01069	0.00727	0.00416	0.00623	0.01808	0.00566
$^{87}Sr/^{86}Sr$ (measured)	0.704612	0.704902	0.705265	0.704599	0.705236	0.704751
$^{87}Sr/^{86}Sr$ std error (2σ)	0.000013	0.000013	0.000013	0.000013	0.000013	0.000013
$^{87}Sr/^{86}Sr$ (1155 Ma)	0.704438	0.704783	0.705197	0.704498	0.704942	0.704659
Sm (ppm)	0.20	0.88	0.14	0.14	0.61	0.18
Nd (ppm)	1.18	6.12	1.06	0.88	3.90	1.20
$^{147}Sm/^{144}Nd$	0.10448	0.08687	0.08212	0.09707	0.09400	0.08909
$^{143}Nd/^{144}Nd$ (measured)	0.512070	0.511879	0.511894	0.512013	0.511958	0.511937
$^{143}Nd/^{144}Nd$ std error (2σ)	0.000013	0.000011	0.000015	0.000013	0.000011	0.000013
$^{143}Nd/^{144}Nd$ (1155 Ma)	0.511280	0.511222	0.511273	0.511279	0.511247	0.511263
ε_{Nd} (1155 Ma)	2.6 ± 0.2	1.5 ± 0.2	2.5 ± 0.3	2.6 ± 0.2	2.0 ± 0.2	2.3 ± 0.3
$\delta^{18}O$ (VSMOW; ‰) (ref 18)	9.07	9.17	10.66	9.07	9.82	9.29
$\delta^{18}O$ std error (2σ; ‰) ref 18)	0.18	0.18	0.12	0.16	0.3	0.26
Boron data in Tables S1 and S2 and EPMA data in Tables S3 and/or S4?	No	No	Yes	No	No	Yes

Larger tables are included in a .zip file:

Table S7: Parameters used for Magma Chamber Simulator and Assimilation-Fractional Crystallization (AFC) modelling.
Table S8: Major element, trace element, and isotopic compositions for Marcy and Morin rocks, endmember candidate parental magmas, and lower crustal xenoliths.
Table S9: Assimilation-Fractional Crystallization (AFC) model and outputs.
Table S10: Magma Chamber Simulator run output for candidate parental magma #1.
Table S11: Magma Chamber Simulator run output for candidate parental magma #2.
Table S12: Magma Chamber Simulator run output for candidate parental magma #3.
Table S13: Magma Chamber Simulator run output for candidate parental magma #4.
Table S14: Magma Chamber Simulator run output for candidate parental magma #1 with mafic wallrock.
Table S15: Magma Chamber Simulator run output for candidate parental magma #1 with (meta)sedimentary wallrock.

REFERENCES AND NOTES

1. L. D. Ashwal, *Anorthosites* (Springer-Verlag, 1993), p. 422.
2. P. Sotiriou, A. Polat, Petrogenesis of anorthosites throughout Earth history. *Precambrian Res.* **384**, 106936 (2023).
3. C. Rey-Moral, T. Mochales, E. Merino Martínez, J. L. García Lobón, M. T. López Bahut, R. Martín-Banda, M. C. Feria, D. Ballesteros, A. Machadinho, D. Alves, Recording the largest gabbro-anorthositic complex worldwide: The Kunene Complex (KC), SW Angola. *Precambrian Res.* **379**, 106790 (2022).
4. L. D. Ashwal, G. M. Bybee, Crustal evolution and the temporality of anorthosites. *Earth Sci. Rev.* **173**, 307–330 (2017).
5. C. O'Neill, M. Brown, B. Schaefer, J. A. Gazi, Earth's anomalous middle-age magmatism driven by plate slowdown. *Sci. Rep.* **12**, 10460 (2022).
6. N. M. W. Roberts, J. Salminen, Å. Johansson, R. N. Mitchell, R. M. Palin, K. C. Condie, C. J. Spencer, On the enigmatic mid-Proterozoic: Single-lid versus plate tectonics. *Earth Planet. Sci. Lett.* **594**, 117749 (2022).
7. B. Charlier, J.-C. Duchesne, J. Vander Auwera, J.-Y. Storme, R. Maquil, J. Longhi, Polybaric fractional crystallization of high-alumina basalt parental magmas in the Egersund–Ogna massif-type Anorthosite (Rogaland, SW Norway) constrained by plagioclase and high-alumina orthopyroxene Megacrysts. *J. Petrol.* **51**, 2515–2546 (2010).
8. R. Fred, J. S. Heinonen, A. Heinonen, W. A. Bohrson, Thermodynamic constraints on the petrogenesis of massif-type anorthosites and their parental magmas. *Lithos* **422-423**, 106751 (2022).
9. G. M. Bybee, L. D. Ashwal, S. B. Shirey, M. Horan, T. Mock, T. B. Andersen, Pyroxene

megacrysts in Proterozoic anorthosites: Implications for tectonic setting, magma source and magmatic processes at the Moho. *Earth Planet. Sci. Lett.* **389**, 74–85 (2014).

10. J. W. Valley, J. R. O'Neil, Oxygen isotope evidence for shallow emplacement of Adirondack anorthosite. *Nature* **300**, 497–500 (1982).
11. A. Heinonen, H. Kivisaari, R. M. Michallik, High-aluminum orthopyroxene megacrysts (HAOM) in the Ahvenisto complex, SE Finland, and the polybaric crystallization of massif-type anorthosites. *Contrib. Mineral. Petrol.* **175**, 10 (2020).
12. A. B. Mukherjee, S. Das, D. Sen, B. Bhattacharya, Buoyant rise of anorthosite from a layered basic complex triggered by Rayleigh-Taylor instability: Insights from a numerical modeling study. *Am. Mineral.* **10**, 437–446 (2020).
13. G. M. Bybee, B. Hayes, T. M. Owen-Smith, J. Lehmann, L. D. Ashwal, A. M. Brower, C. M. Hill, F. Corfu, M. Manga, Proterozoic massif-type anorthosites as the archetypes of long-lived (≥100 Myr) magmatic systems—New evidence from the Kunene Anorthosite Complex (Angola). *Precambrian Res.* **332**, 105393 (2019).
14. H. Schiellerup, D. D. Lambert, T. Prestvik, B. Robins, J. S. McBride, R. B. Larsen, Re–Os isotopic evidence for a lower crustal origin of massif-type anorthosites. *Nature* **405**, 781–784 (2000).
15. J. Longhi, A mantle or mafic crustal source for Proterozoic anorthosites? *Lithos* **83**, 183–198 (2005).
16. J. M. McLelland, B. W. Selleck, M. A. Hamilton, M. E. Bickford, Late-to post-tectonic setting of some major Proterozoic anorthosite–mangerite–charnockite–granite (AMCG) suites. *Can. Mineral.* **48**, 729–750 (2010).
17. T. Slagstad, I. H. C. Henderson, N. M. W. Roberts, E. V. Kulakov, M. Ganerød, C. L. Kirkland,

B. Dalslåen, R. A. Creaser, N. Coint, Anorthosite formation and emplacement coupled with differential tectonic exhumation of ultrahigh-temperature rocks in a Sveconorwegian continental back-arc setting. *Precambrian Res.* **376**, 106695 (2022).

18. W. H. Peck, J. W. Valley, Large crustal input to high δ18O anorthosite massifs of the southern Grenville Province: New evidence from the Morin Complex, Quebec. *Contrib. Mineral. Petrol.* **139**, 402–417 (2000).
19. J. M. McLelland, M. E. Bickford, B. M. Hill, C. C. Clechenko, J. W. Valley, M. A. Hamilton, Direct dating of Adirondack massif anorthosite by U-Pb SHRIMP analysis of igneous zircon: Implications for AMCG complexes. *GSA Bulletin* **116**, 1299–1317 (2004).
20. W. H. Peck, B. W. Selleck, S. P. Regan, G. E. Howard, O. O. Kozel, In-situ dating of metamorphism in Adirondack anorthosite. *Am. Mineral.* **103**, 1523–1529 (2018).
21. W. H. Peck, M. P. Quinan, New age constraints on magmatism and metamorphism in the Morin terrane (Grenville Province, Quebec). *Can. J. Earth Sci.* **59**, 232–242 (2022).
22. J. Morrison, J. W. Valley, Contamination of the Marcy Anorthosite Massif, Adirondack Mountains, NY: Petrologic and isotopic evidence. *Contrib. Mineral. Petrol.* **98**, 97–108 (1988).
23. H. W. Jaffe, J. C. Schumacher, Garnet and plagioclase exsolved from aluminum-rich orthopyroxene in the Marcy anorthosite, northeastern Adirondacks, New York. *Can. Mineral.* **23**, 457–478 (1985).
24. H. R. Marschall, "Boron isotopes in the ocean floor realm and the mantle" in *Boron Isotopes–The Fifth Element. Advances in Isotope Geochemistry*, H. R. Marschall, G. L. Foster, Eds. (Springer, 2018), pp. 189–215.
25. C. Martin, K. E. Flores, A. Vitale-Brovarone, S. Angiboust, G. E. Harlow, Deep mantle serpentinization in subduction zones: Insight from in situ B isotopes in slab and mantle wedge serpentinites. *Chem. Geol.* **545**, 119637 (2020).

26. H. R. Marschall, V. D. Wanless, N. Shimizu, P. A. E. Pogge von Strandmann, T. Elliott, B. D. Monteleone, The boron and lithium isotopic composition of mid-ocean ridge basalts and the mantle. *Geochim. Cosmochim. Acta* **207**, 102–138 (2017).

27. S. M. Peacock, R. L. Hervig, Boron isotopic composition of subduction-zone metamorphic rocks. *Chem. Geol.* **160**, 281–290 (1999).

28. H. R. Marschall, R. Altherr, L. Rüpke, Squeezing out the slab—Modelling the release of Li, Be and B during progressive high-pressure metamorphism. *Chem. Geol.* **239**, 323–335 (2007).

29. L. D. Benton, J. G. Ryan, F. Tera, Boron isotope systematics of slab fluids as inferred from a serpentine seamount, Mariana forearc. *Earth Planet. Sci. Lett.* **187**, 273–282 (2001).

30. C. Martin, K. E. Flores, G. E. Harlow, Boron isotopic discrimination for subduction-related serpentinites. *Geology* **44**, 899–902 (2016).

31. J. C. M. De Hoog, E. Clarke, K. Hattori, Mantle wedge olivine modifies slab-derived fluids: Implications for fluid transport from slab to arc magma source. *Geology* **51**, 663–667 (2023).

32. C. Martin, K. E. Flores, G. E. Harlow, S. Angiboust, F. Hodel, G. L. Guice, The B isotopic signature of serpentine from obducted ophiolites: Mixing of fluids and tectonic implications. *Lithos* **456-457**, 107275 (2023).

33. E. F. Rose, N. Shimizu, G. D. Layne, T. L. Grove, Melt production beneath Mt. Shasta from Boron Data in primitive melt inclusions. *Science* **293**, 281–283 (2001).

34. J. M. McLelland, L. Ashwal, L. Moore, Composition and petrogenesis of oxide-, apatite-rich gabbronorites associated with Proterozoic anorthosite massifs: Examples from the Adirondack Mountains, New York. *Contrib. Mineral. Petrol.* **116**, 225–238 (1994).

35. K. E. Seifert, R. F. Dymek, P. R. Whitney, L. A. Haskin, Geochemistry of massif anorthosite and associated rocks, Adirondack Mountains, New York. *Geosphere* **6**, 855–899 (2010).

36. E. R. Pogue, “Petrogenesis of the Morin anorthosite: Grenville Province, Quebec,” thesis, Washington Univ., St. Louis, MO (1999).

37. S. R. Bohlen, E. J. Essene, Igneous pyroxenes from metamorphosed anorthosite massifs. *Contrib. Mineral. Petrol.* **65**, 433–442 (1978).

38. L. D. Ashwal, J. L. Wooden, Sr and Nd isotope geochronology, geologic history, and origin of the Adirondack Anorthosite. *Geochim. Cosmochim. Acta* **47**, 1875–1885 (1983).

39. W. H. Peck, J. W. Valley, L. Corriveau, A. Davidson, J. McLelland, D. A. Farber, Oxygen-isotope constraints on terrane boundaries and origin of 1.18–1.13 Ga granitoids in the southern Grenville province. *Memoirs* **197**, 163–182 (2004).

40. D. J. DePaolo, Neodymium isotopes in the Colorado Front Range and crust–mantle evolution in the Proterozoic. *Nature* **291**, 193–196 (1981).

41. W. H. Peck, C. C. Clechenko, M. A. Hamilton, J. W. Valley, Oxygen isotopes in the Grenville and Nain AMCG suites: Regional aspects of the crustal component in massif anorthosites. *Can. Mineral.* **48**, 763–786 (2010).

42. I. N. Bindeman, V. V. Ponomareva, J. C. Bailey, J. W. Valley, Volcanic arc of Kamchatka: A province with high-δ 18O magma sources and large-scale 18O/16O depletion of the upper crust. *Geochim. Cosmochim. Acta* **68**, 841–865 (2004).

43. R. T. Gregory, H. P. Taylor Jr., An oxygen isotope profile in a section of Cretaceous Oceanic Crust, Samail Ophiolite, Oman: Evidence for δ18O buffering of the oceans by deep (>5 km) seawater-hydrothermal circulation at mid-ocean ridges. *J. Geophys. Res.* **86**, 2737–2755 (1981).

44. V. S. Papezik, Geochemistry of some Canadian anorthosites. *Geochim. Cosmochim. Acta* **29**, 678–709 (1965).

45. K. E. Seifert, A. F. Voigt, M. F. Smith, W. A. Stensland, Rare earths in the Marcy and Morin

anorthosite complexes. *Can. J. Earth Sci.* **14**, 1033–1045 (1977).

46. D. Demaiffe, D. Weis, J. Michot, J. C. Duchesne, Isotopic constraints on the genesis of the Rogaland anorthositic suite (southwest Norway). *Chem. Geol.* **57**, 167–179 (1986).

47. D. J. Geist, C. D. Frost, A. Kolker, Sr and Nd isotopic constraints on the origin of the Laramie Anorthosite Complex Wyoming. *Am. Mineral.* **75**, 13–20 (1990).

48. R. F. Emslie, M. A. Hamilton, R. J. Thériault, Petrogenesis of a mid-Proterozoic anorthosite-mangerite-charnockite-granite (AMCG) complex: Isotopic and chemical evidence from the Nain Plutonic Suite. *J. Geol.* **102**, 539–558 (1994).

49. P. Gleißner, K. Drüppel, R. L. Romer, The role of crustal contamination in massif-type anorthosites, new evidence from Sr-Nd-Pb isotopic composition of the Kunene Intrusive Complex, NW Namibia. *Precambrian Res.* **185**, 18–36 (2011).

50. A. Heinonen, T. Andersen, O. T. Rämö, M. J. Whitehouse, The source of Proterozoic anorthosite and rapakivi granite magmatism: Evidence from combined in situ Hf–O isotopes of zircon in the Ahvenisto complex, southeastern Finland. *J. Geol. Soc. London* **172**, 103–112 (2015).

51. W. A. Bohrson, F. J. Spera, J. S. Heinonen, G. A. Brown, M. A. Scruggs, J. V. Adams, M. K. Takach, G. Zeff, E. Suikkanen, Diagnosing open-system magmatic processes using the Magma Chamber Simulator (MCS): Part I—Major elements and phase equilibria. *Contrib. Mineral. Petrol.* **175**, 104 (2020).

52. J. S. Heinonen, W. A. Bohrson, F. J. Spera, G. A. Brown, M. A. Scruggs, J. V. Adams, Diagnosing open-system magmatic processes using the Magma Chamber Simulator (MCS): Part II—Trace elements and isotopes. *Contrib. Mineral. Petrol.* **175**, doi: 10.1007/s00410-020-01718-9 (2020).

53. D. J. DePaolo, Trace element and isotopic effects of combined wallrock assimilation and fractional crystallization. *Earth Planet. Sci. Lett.* **53**, 189–202 (1981).

54. C.-T. A. Lee, T. C. Lee, C.-T. Wu, Modeling the compositional evolution of recharging, evacuating, and fractionating (REFC) magma chambers: Implications for differentiation of arc magmas. *Geochim. et Cosmochim. Acta* **143**, 8–22 (2014).

55. G. A. Snyder, L. A. Taylor, G. Crozaz, A. N. Halliday, B. L. Beard, V. N. Sobolev, N. V. Sobolev, The origins of Yakutian eclogite xenoliths. *J. Petrol.* **38**, 85–113 (1997).

56. P. D. Kempton, R. S. Harmon, Oxygen isotope evidence for large-scale hybridization of the lower crust during magmatic underplating. *Geochim. et Cosmochim. Acta* **56**, 971–986 (1992).

57. M. Pertermann, M. M. Hirschmann, Anhydrous partial melting experiments on MORB-like eclogite: Phase relations, phase compositions and mineral–melt partitioning of major elements at 2–3 GPa. *J. Petrol.* **44**, 2173–2201 (2003).

58. C. Kuebler, A. Simonetti, S. S. Simonetti, R. F. Martin, Boron isotope compositions establish the origin of marble from metamorphic complexes: Québec, New York, and Sri Lanka. *Am. Mineral.* **107**, 15–30 (2022).

59. P. R. Phelps, C.-T. A. Lee, Extreme lithium isotope fractionation in quartz from the Stewart pegmatite. *Geochim. et Cosmochim. Acta* **336**, 208–218 (2022).

60. J. J. Ague, J. A. Axler, Interface coupled dissolution-reprecipitation in garnet from subducted granulites and ultrahigh-pressure rocks revealed by phosphorous, sodium, and titanium zonation. *Am. Mineral.* **101**, 1696–1699 (2016).

61. D. S. Keller, J. J. Ague, High-pressure granulite facies metamorphism (~1.8 GPa) revealed in silica-undersaturated garnet-spinel-corundum gneiss, Central Maine Terrane, Connecticut, U.S.A. *Am. Mineral.* **103**, 1851–1868 (2018).

62. R. L. Hervig, G. M. Moore, L. B. Williams, S. M. Peacock, J. R. Holloway, K. Roggensack, Isotopic and elemental partitioning of boron between hydrous fluid and silicate melt. *Am. Mineral.* **87**, 769–774 (2002).

63. U. Hålenius, H. Skogby, M. Edén, S. Nazzareni, P. Kristiansson, J. Resmark, Coordination of boron in nominally boron-free rock forming silicates: Evidence for incorporation of BO3 groups in clinopyroxene. *Geochim. et Cosmochim. Acta* **74**, 5672–5679 (2010).

64. B. Wunder, J. Stefanski, R. Wirth, M. Gottschalk, Al-B substitution in the system albite (NaAlSi3O8)–reedmergnerite (NaBSi3O8). *Eur. J. Mineral.* **25**, 499–508 (2013).

65. J. C. M. De Hoog, I. P. Savov, "Boron isotopes as a tracer of subduction zone processes" in *Boron Isotopes–The Fifth Element. Advances in Isotope Geochemistry*, H. R. Marschall, G. L. Foster, Eds. (Springer, 2018), pp. 217–247.

66. Z. Huang, C. Yuan, X. Long, Y. Zhang, X. Ma, J. Soldner, L. Du, C. Shu, The cause for Nuna breakup in the early to middle mesoproterozoic. *Precambrian Res.* **362**, 106287 (2022).

67. P. A. Brandl, M. Regelous, C. Beier, K. M. Haase, High mantle temperatures following rifting caused by continental insulation. *Nat. Geosci.* **6**, 391–394 (2013).

68. J. M. McLelland, J. Chiarenzelli, Isotopic constraints on emplacement age of anorthositic rocks of the Marcy massif, Adirondack Mts., New York. *J. Geol.* **98**, 19–41 (1989).

69. W. H. Peck, Reconnaissance geochronology and geochemistry of the Mont-Tremblant gneiss of the Morin terrane, Grenville Province Québec. *Geosphere* **8**, 1356–1365 (2012).

70. W. H. Peck, B. W. Selleck, M. S. Wong, J. R. Chiarenzelli, K. S. Harpp, K. Hollocher, J. S. Lackey, J. Catalano, S. P. Regan, A. Stocker, Orogenic to postorogenic (1.20–1.15 Ga) magmatism in the Adirondack Lowlands and Frontenac terrane, southern Grenville Province, USA and Canada. *Geosphere* **9**, 1637–1663 (2013).

71. L. D. Ashwal, Mineralogy of mafic and Fe–Ti oxide-rich differentiates of the Marcy anorthosite massif, Adirondacks New York. *Am. Mineral.* **67**, 14–27 (1982).

72. I. N. Bindeman, J. M. Eiler, G. M. Yogodzinski, Y. Tatsumi, C. R. Stern, T. L. Grove, M. Portnyagin, K. Hoernle, L. V. Danyushevsky, Oxygen isotope evidence for slab melting in modern and ancient subduction zones. *Earth Planet. Sci. Lett.* **235**, 480–496 (2005).

73. S. J. Turner, C. H. Langmuir, Sediment and ocean crust both melt at subduction zones. *Earth Planet. Sci. Lett.* **584**, 117424 (2022).

74. C. Herzberg, K. Condie, J. Korenaga, Thermal history of the Earth and its petrological expression. *Earth Planet. Sci. Lett.* **292**, 79–88 (2010).

75. R. M. Palin, M. Santosh, W. Cao, S.-S. Li, D. Hernández-Uribe, A. Parsons, Secular change and the onset of plate tectonics on Earth. *Earth Sci. Rev.* **207**, 103172 (2020).

76. C. J. Hawkesworth, P. A. Cawood, B. Dhuime, The evolution of the continental crust and the onset of plate tectonics. *Front. Earth Sci.* **8**, 326 (2020).

77. W. H. Peck, "Oxygen isotope studies of Grenville metamorphism and magmatism," thesis, Univ. of Wisconsin, Madison, WI (2000).

78. W. H. Peck, B. W. Selleck, J. W. Valley, M. J. Spicuzza, A. T. Taylor, Emplacement and metamorphism of the Marcy anorthosite: New constraints from geochronology and oxygen isotopes. *Geol. Soc. Am. Abstr. Programs* **49**, doi: 10.1130/abs/2017AM-299676 (2017).

79. H. R. Marschall, B. D. Monteleone, Boron isotope analysis of silicate glass with very low boron concentrations by secondary ion mass spectrometry. *Geostand. Geoanal. Res.* **39**, 31–46 (2014).

80. M. Chaussidon, F. Robert, D. Mangin, P. Hanon, E. F. Rose, Analytical procedures for the measurement of boron isotope compositions by ion microprobe in meteorites and mantle rocks. *Geostand. Newsl.* **21**, 7–17 (1997).

81. S. Kasemann, A. Meixner, A. Rocholl, T. Vennemann, M. Rosner, A. K. Schmitt, M. Wiedenbeck, Boron and oxygen isotope composition of certified reference materials NIST SRM 610/612 and reference materials JB-2 and JR-2. *Geostand. Newsl.* **25**, 405–416 (2001).

82. C. Martin, E. Ponzereva, G. Harlow, In situ lithium and boron isotope determinations in mica, pyroxene, and serpentine by LA-MC-ICP-MS. *Chem. Geol.* **412**, 107–116 (2015).

83. E. J. Catanzaro, *Boric Acid: Isotopic and Assay Standard Reference Materials* (National Bureau of Standards, Institute for Materials Research, 1970).

84. J.-I. Kimura, Q. Chang, T. Ishikawa, T. Tsujimori, Influence of laser parameters on isotope fractionation and optimisation of lithium and boron isotope ratio measurements using laser ablation-multiple Faraday collector-inductively coupled plasma mass spectrometry. *J. Anal. At. Spectrom* **31**, 2305–2320 (2016).

85. K. P. Jochum, S. A. Wilson, W. Abouchami, M. Amini, J. Chmeleff, A. Eisenhauer, E. Hegner, L. M. Iaccheri, B. Kieffer, J. Krause, W. F. McDonough, R. Mertz-Kraus, I. Raczek, R. L. Rudnick, D. Scholz, G. Steinhoefel, B. Stoll, A. Stracke, S. Tonarini, D. Weis, U. Weis, J. D. Woodhead, GSD-1G and MPI-DIN G reference glasses for in situ and bulk isotopic determination. *Geostand. Geoanal. Res.* **35**, 193–226 (2011).

86. J. W. Valley, N. Kitchen, M. J. Kohn, C. R. Niendorf, M. J. Spicuzza, UWG-2, a garnet standard for oxygen isotope ratios: Strategies for high precision and accuracy with laser heating. *Geochim. et Cosmochim. Acta* **59**, 5223–5231 (1995).

87. T. Tanaka, S. Togashi, H. Kamioka, H. Amakawa, H. Kagami, T. Hamamoto, M. Yuhara, Y. Orihashi, S. Yoneda, H. Shimizu, T. Kunimaru, K. Takahashi, T. Yanagi, T. Nakano, H. Fujimaki, R. Shinjo, Y. Asahara, M. Tanimizu, C. Dragusanu, JNdi-1: A neodymium isotopic reference in consistency with LaJolla neodymium. *Chem. Geol.* **168**, 279–281 (2000).

88. D. Weis, B. Kieffer, C. Maerschalk, J. Barling, J. de Jong, G. A. Williams, D. Hanano, W. Pretorius, N. Mattielli, J. S. Scoates, A. Goolaerts, R. M. Friedman, J. B. Mahoney, High-precision isotopic characterization of USGS reference materials by TIMS and MC-ICP-MS. *Geochem. Geophys. Geosyst.* **7**, Q08006 (2006).

89. I. M. Villa, N. E. Holden, A. Possolo, R. B. Ickert, D. B. Hibbert, P. R. Renne, IUPAC-IUGS recommendation on the half-lives of 147Sm and 146Sm. *Geochim. et Cosmochim. Acta* **285**, 70–77 (2020).

90. I. M. Villa, P. De Bièvre, N. E. Holden, P. R. Renne, IUPAC-IUGS recommendation on the half life of 87Rb. *Geochim. et Cosmochim. Acta* **164**, 382–385 (2015).

91. A. Bouvier, J. D. Vervoort, P. J. Patchett, The Lu–Hf and Sm–Nd isotopic composition of CHUR: Constraints from unequilibrated chondrites and implications for the bulk composition of terrestrial planets. *Earth Planet. Sci. Lett.* **273**, 48–57 (2008).

92. R. M. Gaschnig, J. D. Vervoort, R. S. Lewis, B. Tikoff, Isotopic evolution of the Idaho batholith and challis intrusive province northern US Cordillera. *J. Petrol.* **52**, 2397–2429 (2011).

93. T. A. Johnson, J. D. Vervoort, M. J. Ramsey, J. N. Aleinikoff, S. Southworth, Constraints on the timing and duration of orogenic events by combined Lu–Hf and Sm–Nd geochronology: An example from the Grenville orogeny. *Earth Planet. Sci. Lett.* **501**, 152–164 (2018).

94. M. S. Ghiorso, R. O. Sack, Chemical mass transfer in magmatic processes IV. A revised and internally consistent thermodynamic model for the interpolation and extrapolation of liquid-solid equilibria in magmatic systems at elevated temperatures and pressures. *Contrib. Mineral. Petrol.* **119**, 197–212 (1995).

95. G. A. R. Gualda, M. S. Ghiorso, R. V. Lemons, T. L. Carley, Rhyolite-MELTS: A modified calibration of MELT S optimized for silica-rich, Fluid-bearing Magmatic Systems. *J. Petrol.* **53**, 875–890 (2012).

96. M. S. Ghiorso, G. A. R. Gualda, An H2O–CO2 mixed fluid saturation model compatible with rhyolite-MELTS. *Contrib. Mineral. Petrol.* **169**, 53 (2015).

97. R. L. Rudnick, W. F. McDonough, M. T. McCulloch, S. R. Taylor, Lower crustal xenoliths from Queensland, Australia: Evidence for deep crustal assimilation and fractionation of continental basalts. *Geochim. Cosmochim. Acta* **50**, 1099–1115 (1986).

98. H.-G. Stosch, G. W. Lugmair, H. A. Seck, Geochemistry of granulite-facies lower crustal xenoliths: Implications for the geological history of the lower continental crust below the Eifel, West Germany. *Geol. Soc. Spec. Publ.* **24**, 309–317 (1986).

99. R. L. Rudnick, S. R. Taylor, The composition and petrogenesis of the lower crust: A xenolith study. *J. Geophys. Res.* **92**, 13981–14005 (1987). 100. H. Downes, C. Dupuy, A. F. Leyreloup, Crustal evolution of the Hercynian belt of Western Europe: Evidence from lower-crustal granulitic xenoliths (French Massif Central). *Chem. Geol.* **83**, 209–231 (1990).

101. G. Loock, H.-G. Stosch, H. A. Seck, Granulite facies lower crustal xenoliths from the Eifel, West Germany: Petrological and geochemical aspects. *Contrib. Mineral. Petrol.* **105**, 25–41 (1990).

102. H. Downes, P. D. Kempton, D. Briot, R. S. Harmon, A. F. Leyreloup, Pb and O isotope systematics in granulite facies xenoliths, French Massif Central: Implications for crustal processes. *Earth Planet. Sci. Lett.* **102**, 342–357 (1991).

103. M. T. McCulloch, R. T. Gregory, G. J. Wasserburg, H. P. Taylor Jr., Sm-Nd, Rb-Sr, and 18O/16O isotopic systematics in an oceanic crustal section: Evidence from the Samail ophiolite. *J. Geophys. Res.* **86**, 2721–2735 (1981).

104. H. J. Smith, A. J. Spivack, H. Staudigel, S. R. Hart, The boron isotopic composition of altered oceanic crust. *Chem. Geol.* **126**, 119–135 (1995).

105. M. W. Schmidt, O. Jagoutz, The global systematics of primitive arc melts. *Geochem. Geophys. Geosyst.* **18**, 2817–2854 (2017).

106. D. McKenzie, R. K. O'Nions, Partial melt distributions from inversion of rare Earth element concentrations. *J. Petrol.* **32**, 1021–1091 (1991).

107. C. Boschi, A. Dini, G. L. Früh-Green, D. S. Kelley, Isotopic and element exchange during serpentinization and metasomatism at the Atlantis Massif (MAR 30°N): Insights from B and Sr isotope data. *Geochim. Cosmochim. Acta* **72**, 1801–1823 (2008).

108. F. Vils, S. Tonarini, A. Kalt, H.-M. Seitz, Boron, lithium and strontium isotopes as tracers of seawater-serpentinite interaction at Mid-Atlantic ridge, ODP Leg 209. *Earth Planet. Sci. Lett.* **286**, 414–425 (2009).

109. M. Scambelluri, S. Tonarini, Boron isotope evidence for shallow fluid transfer across subduction zones by serpentinized mantle. *Geology* **40**, 907–910 (2012).

110. C. Boschi, E. Bonatti, M. Ligi, D. Brunelli, A. Cipriani, L. Dallai, M. D'Orazio, G. L. Früh-Green, S. Tonarini, J. D. Barnes, R. M. Bedini, Serpentinization of mantle peridotites along an uplifted lithospheric section, Mid Atlantic Ridge at 11° N. *Lithos* **178**, 3–23 (2013).

111. J. Harvey, C. J. Garrido, I. Savov, S. Agostini, J. A. Padrón-Navarta, C. Marchesi, V. López Sánchez-Vizcaíno, M. T. Gómez-Pugnaire, 11B-rich fluids in subduction zones: The role of antigorite dehydration in subducting slabs and boron isotope heterogeneity in the mantle. *Chem. Geol.* **376**, 20–30 (2014).

112. J. Harvey, I. P. Savov, S. Agostini, R. A. Cliff, R. Walshaw, Si-metasomatism in serpentinized peridotite: The effects of talc-alteration on strontium and boron isotopes in abyssal serpentinites from Hole 1268a, ODP Leg 209. *Geochim. Cosmochim. Acta* **126**, 30–48 (2014).

113. E. Cannaò, S. Agostini, M. Scambelluri, S. Tonarini, M. Godard, B, Sr and Pb isotope geochemistry of high-pressure Alpine metaperidotites monitors fluid-mediated element recycling during serpentinite dehydration in subduction mélange (Cima di Gagnone, Swiss Central Alps). *Geochim. Cosmochim. Acta* **163**, 80–100 (2015).

114. E. Cannaò, M. Scambelluri, S. Agostini, S. Tonarini, M. Godard, Linking serpentinite geochemistry with tectonic evolution at the subduction plate-interface: The Voltri Massif case study (Ligurian Western Alps, Italy). *Geochim. Cosmochim. Acta* **190**, 115–133 (2016).

115. K. Yamaoka, T. Ishikawa, O. Matsubaya, D. Ishiyama, K. Nagaishi, Y. Hiroyasu, H. Chiba, H. Kawahata, Boron and oxygen isotope systematics for a complete section of oceanic crustal rocks in the Oman ophiolite. *Geochim. Cosmochim. Acta* **84**, 543–559 (2012).

116. K. Yamaoka, S. Matsukura, T. Ishikawa, H. Kawahata, Boron isotope systematics of a fossil hydrothermal system from the Troodos ophiolite, Cyprus: Water-rock interactions in the oceanic crust and subseafloor ore deposits. *Chem. Geol.* **396**, 61–73 (2015).

117. E. Cannaò, M. Scambelluri, O. Müntener, B. Putlitz, S. Agostini, Inheritance versus subduction-related δ11B signatures of eclogites: Insights from the Voltri Massif (Ligurian Western Alps, Italy). *Chem. Geol.* **615**, 121218 (2023).

118. M. R. Palmer, Boron-isotope systematics of Halmahera arc (Indonesia) lavas: Evidence for involvement of the subducted slab. *Geology* **19**, 215–217 (1991).

119. T. Ishikawa, E. Nakamura, Origin of the slab component in arc lavas from across-arc variation of B and Pb isotopes. *Nature* **370**, 205–208 (1994).

120. T. Ishikawa, F. Tera, T. Nakazawa, Boron isotope and trace element systematics of the three volcanic zones in the Kamchatka arc. *Geochim. Cosmochim. Acta* **65**, 4523–4537 (2001).

121. S. Tonarini, W. P. Leeman, G. Ferrara, Boron isotopic variations in lavas of the Aeolian volcanic arc, South Italy. *J. Volcanol. Geotherm. Res.* **110**, 155–170 (2001).

122. S. Tonarini, W. P. Leeman, P. T. Leat, Subduction erosion of forearc mantle wedge implicated in the genesis of the South Sandwich Island (SSI) arc: Evidence from boron isotope systematics. *Earth Planet. Sci. Lett.* **301**, 275–284 (2011).

123. H.-Y. Li, X. Li, J. G. Ryan, C. Zhang, Y.-G. Xu, Boron isotopes in boninites document rapid changes in slab inputs during subduction initiation. *Nat. Comm.* **13**, 993 (2022).

124. H.-Y. Li, C. Xie, J. G. Ryan, C.-M. Yang, R.-P. Zhao, C. Zhang, Y.-G. Xu, Slab dehydration and magmatism in the Kurile arc as a function of depth: An investigation based on B-Sr-Nd-Hf isotopes. *Chem. Geol.* **621**, 121373 (2023).

125. T. Ishikawa, E. Nakamura, Boron isotope systematics of marine sediments. *Earth Planet. Sci. Lett.* **117**, 567–580 (1993).

126. G. L. Foster, P. A. E. Pogge von Strandmann, J. W. B. Rae, Boron and magnesium isotopic composition of seawater. *Geochem. Geophys. Geosyst.* **11**, Q08015 (2010).

127. P. J. Le Roux, S. B. Shirey, L. Benton, E. H. Hauri, T. D. Mock, In situ, multiple-multiplier, laser ablation ICP-MS measurement of boron isotopic composition (δ11B) at the nanogram level. *Chem. Geol.* **203**, 123–138 (2004).

128. L. D. Ashwal, The temporality of anorthosites. *Can. Mineral.* **48**, 711–728 (2010).

129. K. C. Condie, R. C. Aster, Refinement of the supercontinent cycle with Hf, Nd and Sr isotopes. *Geosci. Front.* **4**, 667–680 (2013).

130. R. P. Tollo, L. Corriveau, J. McLelland, M. J. Bartholomew, Proterozoic tectonic evolution of the Grenville orogen in North America: An introduction. *Geol. Soc. Am. Mem.* **197**, doi: 10.1130/0-8137-1197-5.1 (2004).

131. D. W. Fisher, Y. W. Isachsen, L. V. Rickard, Geologic Map of New York State, consisting of sheets: Niagara, Finger Lakes, Hudson-Mohawk, Adirondack, and Lower Hudson: New York State Museum and Science Service, Map and Chart Series No. 15, scale 1:250,000 (1970).